ELSEVIER

Surface and Coatings Technology 108–109 (1998) 114–120

SURFACE & COATINGS TECHNOLOGY

Sintering and creep behavior of plasma-sprayed zirconia- and hafnia-based thermal barrier coatings

Dongming Zhu*, Robert A. Miller

National Aeronautics and Space Administration, Lewis Research Center, Cleveland, OH 44135, USA

Abstract

The sintering and creep of plasma-sprayed ceramic thermal barrier coatings under high temperature conditions are complex phenomena. Changes in thermomechanical and thermophysical properties and in the stress response of these coating systems as a result of the sintering and creep processes are detrimental to coating thermal fatigue resistance and performance. In this paper, the sintering characteristics of ZrO_2–8wt%Y_2O_3, ZrO_2–25wt%CeO_2–2.5wt%Y_2O_3, ZrO_2–6w%NiO–9wt%Y_2O_3, ZrO_2–6wt%Sc_2O_3–2wt%Y_2O_3 and HfO_2–27wt%Y_2O_3 coating materials were investigated using dilatometry. It was found that the HfO_2–Y_2O_3 and baseline ZrO_2–Y_2O_3 exhibited the best sintering resistance, while the NiO-doped ZrO_2–Y_2O_3 showed the highest shrinkage strain rates during the tests. Higher shrinkage strain rates of the coating materials were also observed when the specimens were tested in Ar+5%H_2 as compared to in air. This phenomenon was attributed to an enhanced metal cation interstitial diffusion mechanism under the reducing conditions. It is proposed that increased chemical stability of coating materials will improve the material sintering resistance.

Keywords: Thermal barrier coatings; Ceramic sintering and creep; Defect structure; Dilatometry

1. Introduction

Plasma-sprayed ceramic thermal barrier coatings are being developed for advanced gas turbine and diesel engine applications to improve engine reliability and efficiency. Since these coatings are experiencing severe thermomechanical cycling during engine operation, it is especially challenging to develop coating systems with high reliability and durability. In particular, ceramic coating sintering and creep at high temperature are among the most important issues for the development of advanced thermal barrier coatings, as has been recognized by many investigators [1–10]. The ceramic sintering and creep at high temperature can result in coating shrinkage and through-thickness cracking during cooling, thereby further accelerating the coating failure process. Sintering–segmentation-enhanced delamination can be an important failure mechanism for a thermal barrier coating system, due to stress concentration from the through-thickness cracks, and increased coating elastic modulus from the sintering densification process. The increase in coating thermal conductivity is also detrimental to coating performance. Research efforts involving various techniques have also been made in characterizing the ceramic coating sintering and creep behavior at high temperature and under temperature gradients simulating those encountered in the engine [1,2,7,11–13].

The sintering and creep of plasma-sprayed, porous and microcracked ceramic thermal barrier coatings are complex phenomena. The early work by Firestone et al. [1,2] indicated that the ceramic creep appeared to be a thermally activated process, with the ceramic splat-sliding being an important creep deformation mechanism. More recently, it has been reported that the ceramic thermal barrier coatings can sinter and creep significantly under compressive stress states at relatively low temperatures [11,13,14]. The 'creep' of plasma-sprayed ZrO_2–8wt%Y_2O_3 at room temperature has also been observed at a tensile stress of 7.4 MPa [15]. A mechanism-based model has been proposed to describe the densification and deformation occurring in thermal barrier coatings at temperature by taking into account the thermally and stress-activated diffusion, and the mechanical compacting processes [13]. The dopants in the ceramic coatings can significantly modify the point defect and microstructures in the bulk, at splat–grain boundaries and microcrack surfaces of the materials, thereby can significantly affect these sintering and creep processes. A better understanding of the dopant effects will help to develop future advanced, sintering/creep-resistant 'superalloy-type' ceramic coatings.

*Corresponding author. Ohio Aerospace Institute, NASA Lewis Research Center. Tel.: +1-216-4335422; fax: +1-216-4335544; e-mail: Dongming.Zhu@lerc.nasa.gov

The purpose of this paper is to investigate sintering kinetics of several zirconia- and hafnia-based ceramic coating materials. The ceramic materials investigated include: (a) ZrO_2–8wt%Y_2O_3, a NASA–Lewis Research Center reference (or baseline) material; (b) ZrO_2–25wt%CeO_2–2.5wt%Y_2O_3, a commercially available coating material developed for hot corrosion resistance; (c) HfO_2–27wt%Y_2O_3, a potential new coating material developed at NASA for high temperature stability [16]; (d) ZrO_2–6wt%NiO–9wt%Y_2O_3, a NiO-doped ZrO_2–Y_2O_3 coating material reported to suppress the tetragonal–monoclinic phase transformation [17]; (e) ZrO_2–6wt%Sc_2O_3–2wt%Y_2O_3, developed for improved hot corrosion resistance [18]. The coating sintering and creep mechanisms and dopant effect on coating sintering rates are discussed based on experimental observations and possible defect reactions.

2. Experimental materials and methods

The five ceramic coating materials mentioned above, ZrO_2–8wt%Y_2O_3, ZrO_2–25wt%CeO_2–2.5wt%Y_2O_3, ZrO_2–6wt%NiO–9wt%Y_2O_3, ZrO_2–6wt%Sc_2O_3–2wt%Y_2O_3 and HfO_2–27wt%Y_2O_3, were chosen for this study. The actual compositions of these materials were close to the their nominal compositions. Each of the above materials was prepared by sintering and crushing except for ZrO_2–25CeO_2–2.5wt%Y_2O_3 which was spray dried and plasma spheroidized. A single set of standard plasma-spray parameters was used for each material. The powders with an average particle size of 60 μm of these coating materials were first plasma-sprayed onto 3-mm diameter graphite cylindrical bars, using the plasma spray conditions described previously [19]. The coating thickness was about 0.76 mm, and porosity was about 10%. The graphite bars were then slowly burnt off at 600°C for 6 h in a furnace in air. The hollow ceramic cylinders were cut into 25.4-mm dilatometer specimens.

Ceramic sintering experiments were carried out in air and in Ar+5%H_2 within the temperature range of 900–1400°C, using a UNITHERM™ high temperature dilatometer system shown in Fig. 1. Since the push rod in the dilatometer exerts a certain amount of force (measured at approximately 450 g using a spring device) on the specimen, a uniaxial stress of approximately 0.5 MPa was acting on the specimen during the entire sintering test. Therefore, this experiment can also be considered a low constant-stress creep test for the ceramic materials. During the sintering/creep experiments at various test temperatures, all specimens were heated at a rate of 5°C/min and held at the given test temperature for 15 h, and then cooled down at a rate of 5°C/min to room temperature. Specimen shrinkage during the heating/cooling cycles was continuously recorded in a computer system. Surface morphology changes of the specimens due to the sintering process were examined using a scanning electron microscope (SEM). Phase structures of the specimens before and after dilatometer sintering tests were also examined by X-ray diffractometry with Cu Kα radiation.

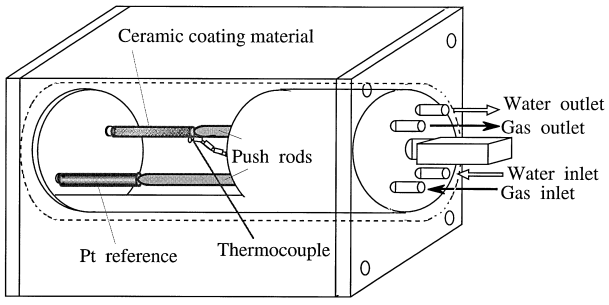

Fig. 1. Schematic diagram showing the ceramic sintering experiment using dilatometry.

3. Experimental results

Fig. 2 shows thermal expansion (shrinkage) results for the coating materials during the sintering experiments at various temperatures measured by the dilatometry technique. Sintering shrinkage was observed for all materials when the specimens were held at temperature for 15 h. The shrinkage strains increased with increasing temperature. It can be seen that the HfO_2–27wt%Y_2O_3 showed the best sintering resistance. In contrast, CeO_2-, Sc_2O_3-, and NiO-doped ZrO_2–Y_2O_3 materials exhibited significant sintering shrinkage. Below the temperature of 900°C, no significant shrinkage strains were detected for the given test time. Fig. 3 illustrates the sintering shrinkage strains occurring at the isothermal sintering stages as a function of temperature.

The sintering rates of the ceramic materials at the isothermal stages change with time, especially at the early sintering time period. As shown in examples in Fig. 4a,b, faster shrinkage rates were observed initially, however, relatively constant rates were observed for longer sintering times. At 1400°C as shown in Fig. 4c, the 'steady-state' sintering rates for ZrO_2–Y_2O_3, ZrO_2–CeO_2–Y_2O_3, ZrO_2–Sc_2O_3–Y_2O_3, ZrO_2–NiO–Y_2O_3, and HfO_2–Y_2O_3 are 2.6×10^{-8}, 3.8×10^{-8}, 8.5×10^{-8} and 6.4×10^{-9}/s, respectively. Fig. 4d shows that for ZrO_2–NiO–Y_2O_3, the second cycle resulted in further shrinkage of the specimen at 1200°C.

Fig. 5 shows the sintering shrinkage kinetics of plasma-sprayed ZrO_2–8wt%Y_2O_3 at 1200°C in air and in Ar+5%H_2. It can be seen that when the specimen was tested in a reducing atmosphere, a faster sintering shrinkage rate was observed. In addition, the ceramic coating material turned black after this Ar+H_2 treatment. Increased sintering rates and darkened color were observed for all other materials under the reduced oxygen partial pressure condition. This may imply that the more defective structure of the materials due to Ar+H_2 sintering would increase the

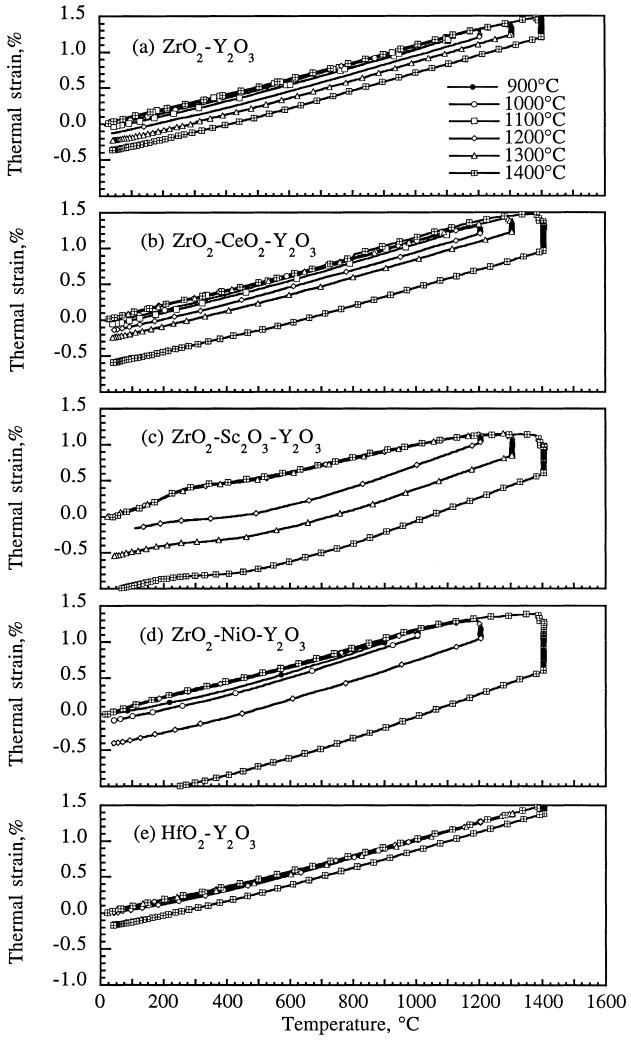

Fig. 2. Thermal expansion and sintering shrinkage response for the coating materials during the dilatometry sintering experiments at various temperatures. (a) ZrO_2–8wt%Y_2O_3; (b) ZrO_2–25wt%CeO_2–2.5wt%Y_2O_3; (c) ZrO_2–6wt%Sc_2O_3–2wt%Y_2O_3; (d) ZrO_2–6wt%NiO–9wt%Y_2O_3; (e) HfO_2–27wt%Y_2O_3.

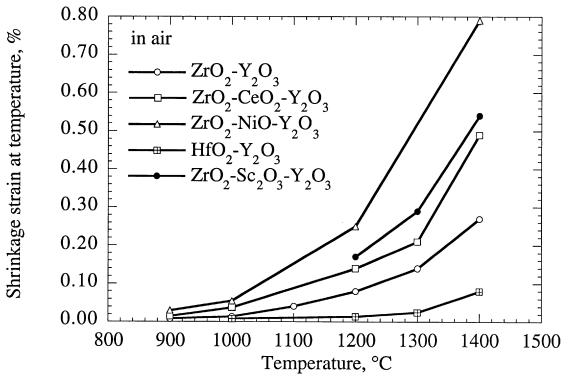

Fig. 3. Total sintering shrinkage strains for the coating materials at the 15-h isothermal sintering stages as a function of temperature.

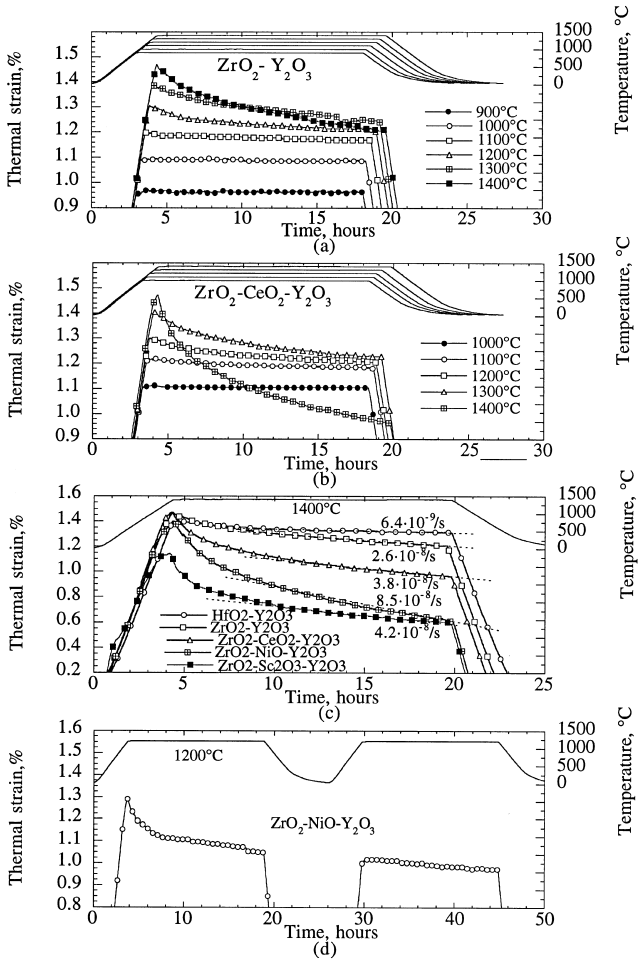

Fig. 4. Sintering behavior of the ceramic materials at the isothermal stages. (a,b) The sintering strains as a function of time and temperature for ZrO_2–8wt%Y_2O_3 and ZrO_2–25wt%CeO_2–2.5wt%Y_2O_3, respectively; (c) steady-state creep rates for the ceramic materials at 1400°C; (d) sintering shrinkage of ZrO_2–6wt%NiO–9wt%Y_2O_3 at 1200°C under two temperature cycles.

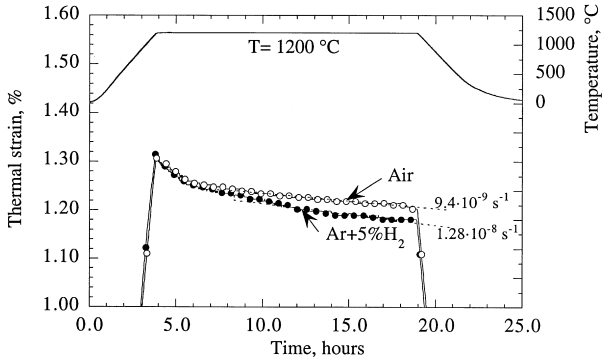

Fig. 5. Sintering shrinkage kinetics of plasma-sprayed ZrO_2–8wt%Y_2O_3 at 1200°C in air and in Ar+5%H_2.

minority defect transport especially at the internal surfaces and grain boundaries, thus resulting in a faster sintering rate.

Fig. 6 illustrates some examples of the X-ray diffraction

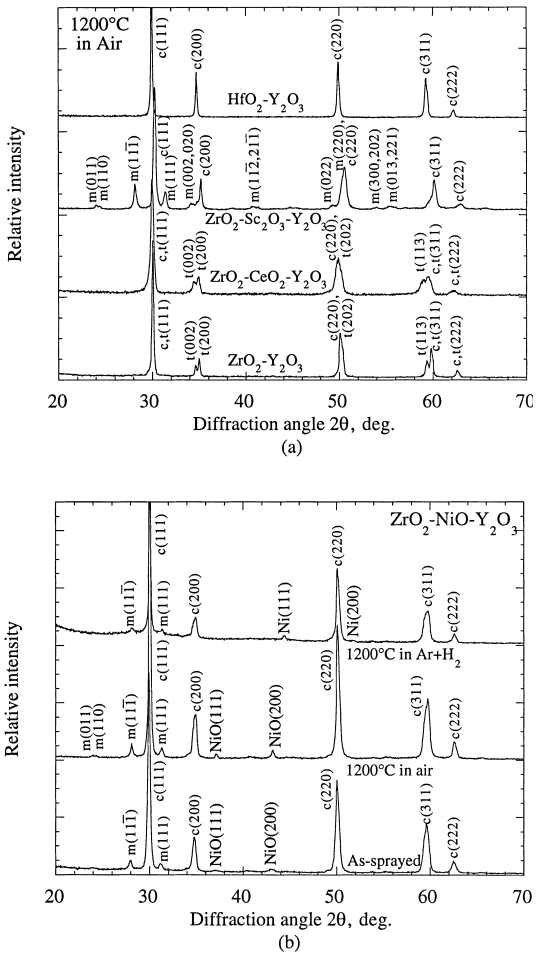

Fig. 6. X-ray diffraction spectra of the plasma-sprayed ceramic coating materials. (a) Diffraction spectra of ZrO_2–Y_2O_3, ZrO_2–CeO_2–Y_2O_3, ZrO_2–Sc_2O_3–Y_2O_3 and HfO_2–Y_2O_3 after 1200°C sintering in air; (b) diffraction spectra of ZrO_2–NiO–Y_2O_3 under the as-sprayed condition, and after 1200°C sintering in air and 1200°C sintering in Ar+5%H_2.

spectra for ZrO_2–Y_2O_3, ZrO_2–CeO_2–Y_2O_3, HfO_2–Y_2O_3 and ZrO_2–Sc_2O_3–Y_2O_3 after 15 h sintering at 1200°C in air. From X-ray diffraction experiments, it was found that the baseline ZrO_2–8wt%Y_2O_3 primarily consisted of tetragonal t′ phase. The CeO_2-doped ZrO_2–Y_2O_3 also showed significant amount of t′ phase; however, the possibility that the cubic c phase might also be increased as compared to the baseline material requires further study. Due to the high concentration of yttria dopant, HfO_2–27wt%Y_2O_3 had a fully stabilized cubic c phase. No appreciable monoclinic phase was observed in these three materials. Heat treatments related to the sintering experiments under various temperature and oxygen pressure conditions did not measurably alter the phase structures of these materials. The as-sprayed ZrO_2–Sc_2O_3–Y_2O_3 material showed tetragonal t′ phase and an increased amount of the monoclinic m phase. The monoclinic phase in the Sc_2O_3-doped materials increased after the sintering tests.

The NiO-doped ZrO_2–Y_2O_3 showed more complex phase structures. As shown in Fig. 6, the majority phase in ZrO_2–NiO–Y_2O_3 was the cubic c phase, instead of tetragonal phase in the baseline material. However, the monoclinic m phase was also present in this material. Because of the limited solubility of NiO in ZrO_2–Y_2O_3 (about 3 mol% at 1600°C [17]), NiO phase was observed in the as-sprayed and air-sintered specimens. In the Ar+H_2 sintered specimens, however, a Ni phase was present because of the reduction of NiO.

Surface microstructure changes were also observed after the sintering experiments. Certain regions showed more noticeable sintering densification and grain growth as compared to other regions, indicating there were some heterogeneities in the observed sintering phenomena. Fig. 7 shows micrographs of ceramic surfaces of the ZrO_2–8wt%Y_2O_3 coating material before and after the dilatometry sintering at 1200°C. It can be seen that sintering which occurred could result in microcrack healing and material densification, accompanying with substantial grain growth in some regions.

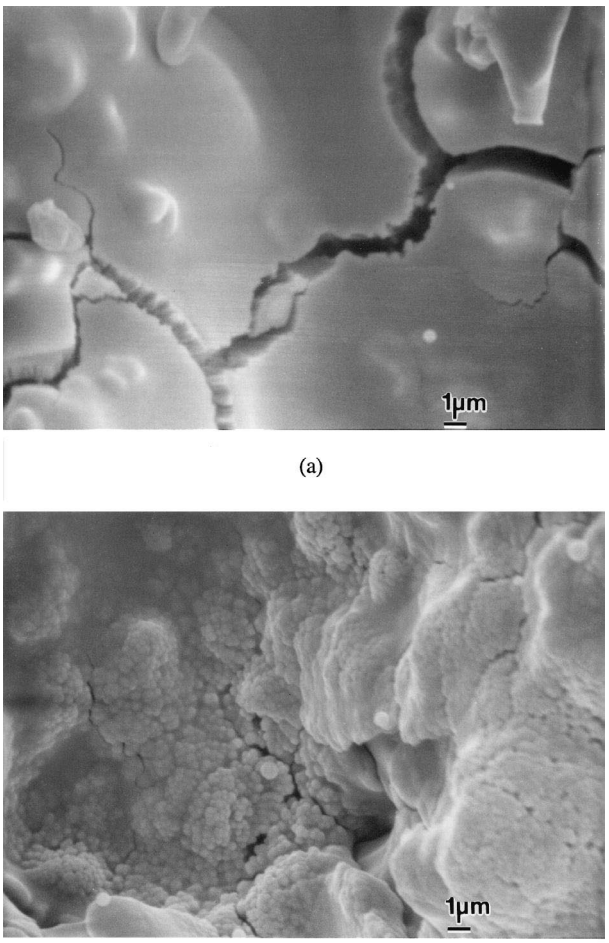

Fig. 7. Surface SEM micrographs of the ZrO_2–8wt%Y_2O_3 ceramic coating material before and after the dilatometry sintering at 1200°C for 15 h. (a) Before the sintering test; (b) after the sintering test.

4. Discussion

The sintering and low-stress creep characteristics of the ceramic coating materials, determined by the dilatometer technique, are similar to the creep behavior of plasma-sprayed coatings obtained from high temperature mechanical creep tests [1,12,20] and the laser sintering/creep test [13]. The fast initial creep rate and low creep activation energy have been attributed to mechanical sliding, fast surface and grain boundary diffusion, and temperature and stress gradient enhanced transport in the porous and weak ceramic coatings [13]. Fig. 8 illustrates the creep rates of the plasma-sprayed ZrO_2–8wt%Y_2O_3 as a function of stress and temperature determined by the laser sintering technique [13]. It can be seen that with higher compressive stresses acting on the coating, a long primary creep stage and substantial sintering/creep rates can be observed at much lower temperatures. In the high temperature, low stress sintering/creep tests by the dilatometer technique, mechanical sliding becomes less predominant, and a nearly 'steady-state' creep region has been reached in a relatively short period of time. Diffusion-related processes become more important mechanisms for the low stress sintering and creep deformation. The observed grain growth phenomena also suggest the complex diffusion occurring during the dilatometer sintering test.

Creep deformation of ceramic coating materials requires diffusion of the cations and anions in these materials. The creep rate in ceramics is therefore determined by the diffusion of the slowest species, diffusing along the fastest path. In yttria-stabilized zirconia, the majority defect types are oxygen vacancies and yttrium aliovalent dopants at normal cation sites. The possible minority defects are zirconia interstitials, zirconium vacancies, and yttrium interstitials, and the zirconium and yttrium cation transport is confirmed to be the slowest process in yttria-stabilized single crystals [21]. The defect reactions in the yttria-stabilized zirconia can be written according to Kröger–Vink notation [22] as

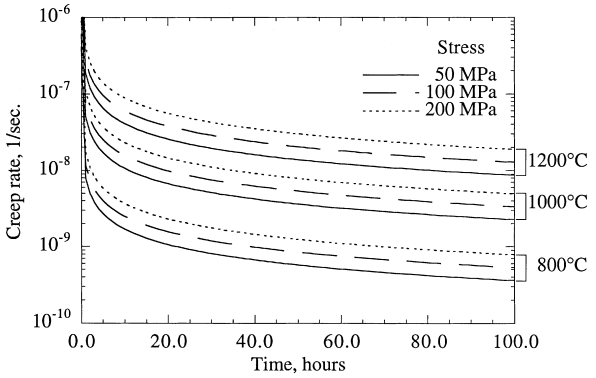

Fig. 8. The coating creep rates of plasma-sprayed ZrO_2–8wt%Y_2O_3, determined by laser high heat flux sintering/creep technique, as a function of stress and temperature.

$$Y_2O_3 = 2Y'_{Zr} + 3O_O^{\times} + V_O^{\cdot\cdot} \quad (1)$$

$$O_O^{\times} = V_O^{\cdot\cdot} + 2e' + \tfrac{1}{2}O_2(g) \quad (2)$$

(for majority defects) and

$$2O_O{}^{\times}Zr_{Zr}{}^{\times} = Zr_i^{\cdot\cdot\cdot\cdot} + 4e' + O_2(g) \quad (3)$$

$$\tfrac{1}{2}O_2(g) = V'_{Zr}{}''' + 4h^{\cdot} \quad (4)$$

(for minority defects)

In the extrinsic region, the majority defect oxygen vacancy concentration $[V_O^{\cdot\cdot}]$ is determined by the dopant yttria concentration $[Y'_{Zr}]$, which follows the electroneutrality condition

$$[Y'_{Zr}] = 2[V_O^{\cdot\cdot}]. \quad (5)$$

At lower oxygen partial pressures in the intrinsic region where the electron conductivity becomes important, oxygen vacancies can be further introduced according to Eq. (2), that is

$$[V_O^{\cdot\cdot}]n^2 = K_{V_O^{\cdot\cdot}} p_{O_2}^{-1/2} \exp\left(-\frac{\Delta H_{V_O^{\cdot\cdot}}}{RT}\right) \quad (6)$$

where n is electron concentration, $K_{V_O^{\cdot\cdot}}$ is reaction constant, $\Delta H_{V_O^{\cdot\cdot}}$ is the enthalpy of formation of oxygen vacancies, R and T are gas constant and temperature, respectively. Metal interstitials can be an important defect type in the oxygen deficient oxide [23], and the zirconium interstitial concentration can be obtained from Eq. (3)

$$[Zr_i^{\cdot\cdot\cdot\cdot}]n^4 = K_{Zr_i^{\cdot\cdot\cdot\cdot}} p_{O_2}^{-1} \exp\left(-\frac{\Delta H_{Zr_i^{\cdot\cdot\cdot\cdot}}}{RT}\right). \quad (7)$$

where $K_{Zr_i^{\cdot\cdot\cdot\cdot}}$ is a constant, $\Delta H_{Zr_i^{\cdot\cdot\cdot\cdot}}$ is the enthalpy of formation of zirconium interstitials. In this intrinsic region, the electroneutrality can be expressed as

$$n = 2[V_O^{\cdot\cdot}] + 4[Zr_i^{\cdot\cdot\cdot\cdot}]. \quad (8)$$

By combining Eqs. (6)–(8), the oxygen vacancy and zirconia interstitial concentrations can be written as

$$[V_O^{\cdot\cdot}] = (K_{V_O^{\cdot\cdot}}/4)^{1/3}\, p_{O_2}^{-1/6} \exp\left(-\frac{\Delta H_{V_O^{\cdot\cdot}}}{3RT}\right) \quad (9a)$$

$$[Zr_i^{\cdot\cdot\cdot\cdot}] = (K_{Zr_i^{\cdot\cdot\cdot\cdot}}/(2K_{V_O^{\cdot\cdot}})^{4/3}) p_{O_2}^{-1/3} \exp\left(-\frac{3\Delta H_{Zr_i^{\cdot\cdot\cdot\cdot}} - 4\Delta H_{V_O^{\cdot\cdot}}}{3RT}\right). \quad (9b)$$

(when $[V_O^{\cdot\cdot}] \gg [Zr_i^{\cdot\cdot\cdot\cdot}]$)

$$[V_O^{\cdot\cdot}] = (K_{V_O^{\cdot\cdot}}/(4K_{Zr_i^{\cdot\cdot\cdot\cdot}})^{2/5}) p_{O_2}^{-1/10} \exp\left(-\frac{5\Delta H_{V_O^{\cdot\cdot}} - 2\Delta H_{Zr_i^{\cdot\cdot\cdot\cdot}}}{5RT}\right) \quad (10a)$$

$$[Zr_i^{\cdot\cdot\cdot\cdot}] = (K_{Zr_i^{\cdot\cdot\cdot\cdot}}/256)^{1/5} p_{O_2}^{-1/5} \exp\left(-\frac{\Delta H_{Zr_i^{\cdot\cdot\cdot\cdot}}}{5RT}\right). \quad (10b)$$

(when $[V_O^{\cdot\cdot}] \ll [Zr_i^{\cdot\cdot\cdot\cdot}]$)

DOCKET ALARM

Explore Litigation Insights

Docket Alarm provides insights to develop a more informed litigation strategy and the peace of mind of knowing you're on top of things.

Real-Time Litigation Alerts

Keep your litigation team up-to-date with **real-time alerts** and advanced team management tools built for the enterprise, all while greatly reducing PACER spend.

Our comprehensive service means we can handle Federal, State, and Administrative courts across the country.

Advanced Docket Research

With over 230 million records, Docket Alarm's cloud-native docket research platform finds what other services can't. Coverage includes Federal, State, plus PTAB, TTAB, ITC and NLRB decisions, all in one place.

Identify arguments that have been successful in the past with full text, pinpoint searching. Link to case law cited within any court document via Fastcase.

Analytics At Your Fingertips

Learn what happened the last time a particular judge, opposing counsel or company faced cases similar to yours.

Advanced out-of-the-box PTAB and TTAB analytics are always at your fingertips.

API

Docket Alarm offers a powerful API (application programming interface) to developers that want to integrate case filings into their apps.

LAW FIRMS
Build custom dashboards for your attorneys and clients with live data direct from the court.

Automate many repetitive legal tasks like conflict checks, document management, and marketing.

FINANCIAL INSTITUTIONS
Litigation and bankruptcy checks for companies and debtors.

E-DISCOVERY AND LEGAL VENDORS
Sync your system to PACER to automate legal marketing.